Journal of Applied Physics

Strain relaxation in Cu-Al-Ni shape memory alloys studied by *in situ* neutron diffraction experiments

Cite as: J. Appl. Phys. **125**, 082536 (2019); https://doi.org/10.1063/1.5049216
Submitted: 20 July 2018 . Accepted: 27 December 2018 . Published Online: 22 January 2019

I. Ruiz-Larrea, A. López-Echarri, J. F. Gómez-Cortés, M. L. Nó, D. W. Brown, L. Balogh, T. Breczewski, and J. San Juan

openaccess

View Online Export Citation CrossMark

ARTICLES YOU MAY BE INTERESTED IN

Strain measurement of ultrathin epitaxial films using electron diffraction techniques
Journal of Applied Physics **125**, 082401 (2019); https://doi.org/10.1063/1.5049357

Control of magnetic anisotropy in epitaxial Co_2MnAl thin films through piezo-voltage-induced strain
Journal of Applied Physics **125**, 082503 (2019); https://doi.org/10.1063/1.5039430

Effect of strain on the modifications in electronic structure and resistive switching in Ca-doped $BiFeO_3$ films
Journal of Applied Physics **125**, 082510 (2019); https://doi.org/10.1063/1.5045844

Ultra High Performance SDD Detectors

AMETEK MATERIALS ANALYSIS DIVISION

See all our XRF Solutions

© 2019 Author(s).

AIP Publishing

Journal of Applied Physics ARTICLE scitation.org/journal/jap

Strain relaxation in Cu-Al-Ni shape memory alloys studied by *in situ* neutron diffraction experiments

Cite as: J. Appl. Phys. **125**, 082536 (2019); doi: 10.1063/1.5049216
Submitted: 20 July 2018 · Accepted: 27 December 2018 ·
Published Online: 22 January 2019

View Online Export Citation CrossMark

I. Ruiz-Larrea,[1,a)] A. López-Echarri,[2] J. F. Gómez-Cortés,[2] M. L. Nó,[1] D. W. Brown,[3] L. Balogh,[4] T. Breczewski,[1] and J. San Juan[2]

AFFILIATIONS

[1]Departamento de Física Aplicada II, Universidad del País Vasco, UPV/EHU Apdo. 644, 48080 Bilbao, Spain
[2]Departamento de Física de la Materia Condensada, Facultad de Ciencia y Tecnología, Universidad del País Vasco, UPV/EHU Apdo. 644, 48080 Bilbao, Spain
[3]Lujan Neutron Scattering Center, Los Alamos National Laboratory, Los Alamos, New Mexico 87545, USA
[4]Department of Mechanical and Materials Engineering, Queen's University, Kingston, Ontario K7L 3N6, Canada

[a)]**Author to whom correspondence should be addressed:** isabel.ruiz@ehu.es. **Tel.:** +34-94-601-5324

ABSTRACT

In situ neutron diffraction is used to study the strain relaxation on a single crystal and other powdered Cu-Al-Ni shape memory alloys (SMAs) around martensitic transformation temperatures. This work is focused on the analysis of the strain evolution along the temperature memory effect appearing in these alloys after partial thermal transformations. A careful study of the influence of partial cycling on the neutron diffraction spectra in the martensitic phase is presented. Two different effects are observed, the d-spacing position shift and the narrowing of various diffraction peaks, along uncompleted transformation cycles during the thermal reverse martensitic transformation. These changes are associated with the relaxation of the mechanical stresses elastically stored around the martensitic variants, due to the different self-accommodating conditions after uncompleted transformations. The evolution of the stresses is measured through the strain relaxation, which is accessible by neutron diffraction. The observed effects and the measured strain relaxations are in agreement with the predictions of the model proposed to explain this behavior in previous calorimetric studies. In addition, the thermal expansion coefficients of both martensite and austenite phases were measured. The neutron experiments have allowed a complete description of the strains during martensitic transformation, and the obtained conclusions can be extrapolated to other SMA systems.

© 2019 Author(s). *All article content, except where otherwise noted, is licensed under a Creative Commons Attribution (CC BY) license* (http://creativecommons.org/licenses/by/4.0/). https://doi.org/10.1063/1.5049216

I. INTRODUCTION

Shape memory alloys (SMAs) are functional materials characterized by their specific properties of shape memory and superelastic effects, which are based on a reversible first order diffusionless structural phase transition, called martensitic transformation (MT), taking place between the high temperature phase, austenite, and the low temperature phase, martensite, via an atomic lattice shearing responsible for the change of shape.[1–3] Although the main strain associated with the MT is a shearing, it could involve shuffling, distortions, and expansions of the parent phase lattice and consequently important stresses appear in between the two lattices of austenite and martensite. In classical non-thermoelastic MT, these stresses produce intensive plastic deformation around the interfaces and the MT becomes irreversible like in the case of many steels. However, in SMA the MT is thermoelastic, which means that the stresses are accommodated through the formation of multiple martensite domains (or variants) promoting local reversible elastic strains, to minimize the increase of the local stresses and prevent plastic deformation. In spite of that, these self-accommodating groups of martensite are not free of local stresses, which are elastically stored in the lattice of both phases and finally, at the end of the MT, in the martensite lattice. In the absence of any plastic deformation or dissipative processes, the creation of the martensite interfaces and the stored elastic energy are responsible for the hysteresis

© Author(s) 2019

associated with the MT, as well as for the broadening of the transformation temperature range.[4,5] The important point is that the elastic energy stored during the forward MT on cooling constitutes the driving force for the reverse MT on heating, and in the case that such stored elastic energy would be released, the transformation will be accordingly delayed to a higher temperature range. If such evolution occurs, it would constitute an important issue for the reliability of SMA behavior, because the thermal shape memory effect and the recovery of the superelastic effect could be compromised due to the stabilization of the martensite. Indeed, we will shortly describe two effects, apparently associated with this phenomenon, which were reported in the literature.

On the one hand, some size effects were recently reported on the superelastic behavior of SMA at a small scale,[6–8] which are partially attributed to the release of the elastic energy, stored at the growing front of martensites, on the surface of micro and nano pillars. Then, the martensite acquires an improved stability and the stress-induced reverse transformation only happens for very low values during the withdrawal of the stress. On the other hand, several works were published in the last years[9–14] on the so called temperature memory effect (TME), which is characterized by a delay of the thermal reverse MT, which takes place at a higher temperature, after some previous uncompleted heating cycles covering only partially the transformation. Such behavior was first observed in TiNi[15–22] but is also present in Cu-Al-Ni and related alloys.[23,24] To study this effect, calorimetric experiments were usually performed by means of an initial heating run from the martensitic state up to any fixed temperature T_a (known as the "arrested temperature") promoting just a partial reverse MT. After cooling down again to the full martensitic state, the next complete reverse transformation is temperature delayed and a secondary specific heat C_p-peak appears above T_a. The strength and position of this new signal depend on both the percentage of the partial transformation and the number of reiterative previous partial thermal cycles up to T_a, giving place to the originally called "hammer" effect (HE),[25] which enhances the single TME. The reader is referred to a previous work[26] for a detailed description of such thermal effects.

In addition to the experimental works, different theoretical approaches were proposed to explain this phenomenon, and in particular TME was related with dislocations,[17] interface interactions,[20] elastic deformation of the martensitic plates,[16,18] as well as a continuous distribution of the stored elastic energy, whose relaxation is provided by the partial heating cycles.[26] Nevertheless, there is no general agreement on the origin of the described effects, and at present there is a controversy on their physical interpretation, produced by the fact that the evolution of the local stresses cannot be measured, preventing to assess its influence on the transformation behavior. This is also a particularly important technological concern because most of the real SMA actuators usually undergo a partial transformation cycle in working conditions.[1,3]

In this scenario, we propose the following approach: the local stresses and their evolution during MT could be evaluated through the corresponding elastic local lattice strains, which should be accessible by neutron diffraction.

Here, we present new measurements of TME and HE carried out by *in situ* neutron diffraction. These experiments were performed all over the transformation temperature range to obtain information about the microscopic mechanisms underlying the observed behavior. Indeed, measurements of the lattice strains evolution, together with the first time determined thermal expansion coefficients of the martensite phase, permit a global description of the local strain relaxations and contribute to close the controversy about the occurring phenomena.

II. EXPERIMENTAL

Cu-Al-Ni single crystal and powder samples were selected for neutron diffraction experiments because the experiments related to TME,[5,23,26–28] in Cu-Al-Ni alloys, as well as the studies on superelasticity at a small scale,[6–8] gave us a deep experience on the behavior of such alloys. High-purity single crystals were obtained by induction melting and grown by the Stephanov method. They were first annealed at 1170 K for 30 min and then quenched into iced water to retain the parent austenitic β_3 phase. These alloys present a forward MT (on cooling) from the high temperature austenite phase (β_3, cubic $L2_1$, Fm-3m)[29] to the martensite, which depending on the sample composition can be either monoclinic (β'_3, C2/m[30]) or orthorhombic (γ'_3, Pnmm[31]). On the other hand, powder samples of these alloys were synthesized following a previously described procedure.[32,33] The pre-alloyed melt was atomized by using a Leybold Viga 2S with Argon gas at 2.3 MPa. This procedure also replaces the quenching process performed in single crystals. The selected powder particle size for our experiments varies from 100 to 200 μm and each particle contains a few grains. The idea underlying for choosing single crystals and powders of SMA arose because a completely different distribution of martensite size variants could be expected in both kinds of samples, adding more generality to the study. Finally, samples were aged at 353 K for 24 h, in order to stabilize the atomic order, and consequently the MT temperatures,[34] to avoid any further evolution of the MT in working conditions.

A Cu-Al-Ni single crystal with composition Cu (82.3%)-Al (13.7%)-Ni (4%) (wt. %), which will be referred as CAN4, was studied around the martensitic transformation temperature range, from 240 K to 350 K. To make easier a further comparative analysis, the same sample previously used in adiabatic calorimetric measurements was selected for these measurements.[26,35] In addition, the MT of a Cu-Al-Ni powdered sample with composition Cu (83.6%)-Al (13.15%)-Ni (3.25%) (wt. %), which will be referred as CAN19, was also studied from 330 K to 430 K. Previous differential scanning calorimetry (DSC) and adiabatic calorimetric measurements permitted to define these transformation temperature ranges: for CAN4,[26,27] $M_s = 314$ K, $M_f = 262$ K, $A_s = 268$ K, and $A_f = 320$ K; for CAN19,[36] $M_s = 393$ K, $M_f = 353$ K, $A_s = 372$ K, and $A_f = 415$ K (sub-indices s and f account for start and finish temperatures). Both samples show a forward

© Author(s) 2019

transformation from the high temperature austenitic cubic phase (β_3) to the martensitic monoclinic phase (β'_3).

The neutron experiments were performed in the Neutron Powder Diffractometer (NPDF) at the Lujan Neutron Scattering Center in the Los Alamos National Laboratory[37] that uses the data reduction program PDFGETN as well as the programs PDFGUI and DISCUS.[38–40] The instrument operates in time of flight mode receiving neutrons from a tungsten spallation target by means of a proton accelerator. The details of the instrument can be found in the LANL website.

Neutron diffraction patterns were analyzed by the Rietveld method,[41,42] through the refinement of the full pattern using the General Structural Analysis Software (GSAS) developed at the Los Alamos National Laboratory.[43] In the present case, a 4-parameter Pearson-VII function of equation,

$$y = \frac{k_1}{[1 + k_2(x - k_3)^2]^{k_4}}, \quad (1)$$

was used to fit the main peaks. These fits permit to determine the d-peak position (Å), the maximal intensity I_{max} (counts), the peak area A (counts, Å), the full width at half maximum [FWHM (Å)], and the profile parameters (k_1, k_2, k_3, and k_4) characteristic of each peak.[44] CrystalDiffract® software was also used for a general analysis of the data.

In order to study the influence of the thermal partial cycling on the transformation behavior found in these alloys, a similar methodological strategy was selected for both samples. For comparison, the reader can follow a previous work[26] in which the temperature memory effect was studied by calorimetry in the same sample CAN4. The thermal runs were performed at zero stress in a copper vessel under vacuum conditions and are schematically presented in Fig. 1 for the case of sample CAN4.

Measurements start with an initial heating up to the austenite phase (360 K) in order to erase any eventual TME due to previous thermal history. Then, the sample was cooled down to the martensite phase (240 K) and stabilized for 30 min before starting the first complete heating run to obtain the sample reference transformation behavior. This heating is performed by steps in which the complete neutron diffraction pattern is acquired, as indicated in Fig. 1. The fast cooling ramps were done at 10 K/min, whereas the heating ramp to reach the temperature of each step was always programmed at 2 K/min, followed by 10 min holding time to stabilize the temperature. After this holding time, the neutron diffraction measurement started; the time for neutron measurements is not included in the schema of this figure. After cooling down again to the martensitic state, and stabilized at 260 K during 30 min, the sample was ready for the partial cycling up to the arrested intermediate temperature, T_a = 306 K in the case of CAN4 single crystal sample. A similar procedure was used for the powdered CAN19 sample with T_a = 396 K. At these temperatures, both samples show about 50% of the complete MT. The partial cycling study included 6 heating sequences up to T_a, and in all sequences, the neutron diffraction patterns were acquired at different temperature steps. Finally, a last complete run covering the total reverse transformation was done, for comparison with the first complete heating run. Neutron diffraction data were collected only on heating runs, and, to illustrate the acquired patterns, the spectra measured during the first complete heating run are shown in Figs. 2(a) and 2(b), for samples CAN4 and CAN19, respectively.

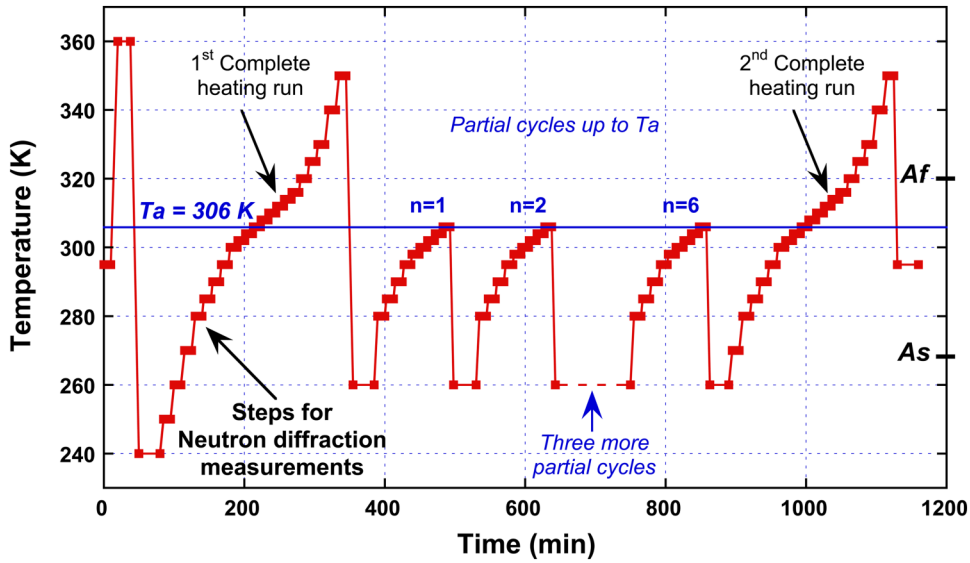

FIG. 1. Schema of the complete sequence of thermal runs during *in situ* neutron diffraction measurements for CAN4 single crystal. The temperature notation is T_a the arrested temperature, A_s the austenitic start temperature, and A_f the austenitic finish temperature.

© Author(s) 2019

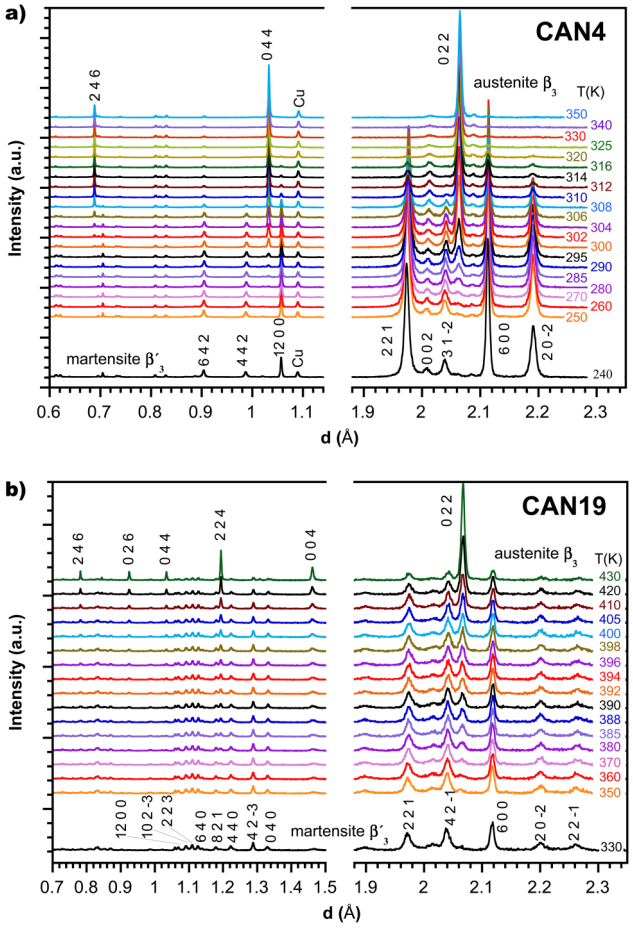

FIG. 2. Neutron diffraction *d*-spectra, which cover the complete martensitic transformation range: (a) CAN4 single crystal and (b) CAN19 powdered sample. The various spectra are shifted up for the sake of clarity. The indexing of several (*h k l*) planes for the martensite β'_3 and the austenite β_3 phases are also included. In the case of CAN4, the reflection from the copper sample vessel is also identified.

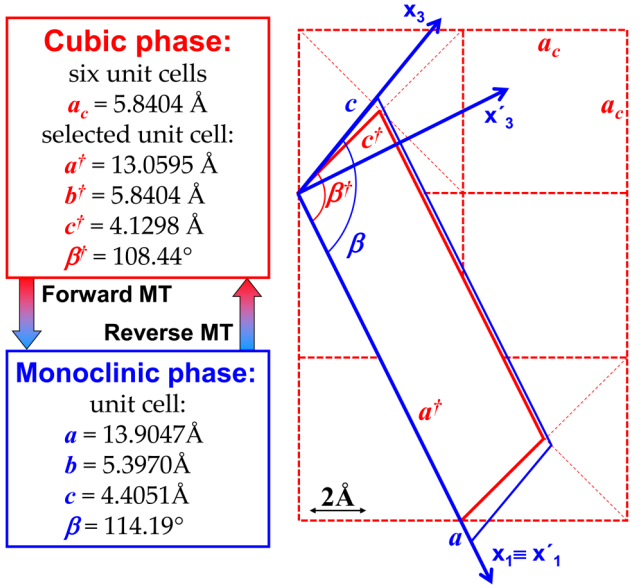

FIG. 3. Schema of cubic (red) and monoclinic (blue) unit cells in the $x_1 - x_3$ plane normal to the binary axis $x_2 = x'_2$ (inwards the page). The orthogonal axis, x'_1 and x'_3, and the lattice parameter values for both phases are also shown. Data for CAN4 single crystal.

III. EXPERIMENTAL RESULTS

A. Lattice parameters

Neutron diffraction collected data during the first complete heating run from 240 K to 350 K for CAN4 single crystal and from 330 K to 430 K for CAN19 powdered sample are presented in Figs. 2(a) and 2(b), respectively. These figures show the observed d-spacing spectra evolution as a function of temperature in the whole temperature range. The indexing of the d_{hkl}-peak positions[45] fit well with the cubic β_3 phase (Fm-3 m)[29] and the martensite β'_3 (C2/m).[30] The conventional crystallographic basis (x_1, x_2, x_3) with x_2 parallel to the monoclinic binary axis was selected, and the smaller monoclinic unit cell was considered according to the standard setting, unique axis *b*, cell choice 1, of the International Crystallographic Tables.[46]

The measured lattice parameters for the two phases in both alloys, CAN4 and CAN19, are shown in Table I, and in Fig. 3, the β'_3 monoclinic cell lattice (blue) is plotted in comparison with the closest cubic one (red) to highlight the monoclinic distortion. These values are similar to those reported for closely related Cu-Al-Ni alloys.[30,33] It must be noted that the measured cell lattice parameters in the martensitic phase have to be seen as average values because, as it will be discussed later, experiments are performed on a

TABLE I. Lattice parameters of austenite and martensite in CAN4 and CAN19 alloys.

			Austenite β_3		Martensite β'_3				
	wt. % Al	wt. % Ni	*T* (K)	*a* (Å)	*T* (K)	*a* (Å)	*b* (Å)	*c* (Å)	β (°)
CAN4	13.70	4.00	320	5.8404	260	13.9047	5.3970	4.4051	114.19
CAN19	13.15	3.25	430	5.8464	330	13.8508	5.3263	4.4160	113.43

© Author(s) 2019

multi-variant martensitic sample showing a strain distribution due to the self-accommodation process.

B. Transformation strain during forward MT

The structural MT from cubic austenite to monoclinic martensite was associated with a strain matrix, accounting for the different strain components ε_i, which is related to the Bain matrix of the MT.[47] In what follows, the strain components ε_i will be calculated and the matrix notation will be fully employed.[48]

As usual, the tensor relations are referred to an orthogonal basis: $[x_1', x_2', x_3']$ in Fig. 3. Then, the strains are calculated from the lattice parameters measured by neutron diffraction,

$$\begin{aligned}
\varepsilon_1 &= \frac{a - a^+}{a^+}, \\
\varepsilon_2 &= \frac{b - b^+}{b^+}, \\
\varepsilon_3 &= \frac{c - c^+ \cdot [1 + \varepsilon_1 \cdot \cos^2(\beta^+) + \varepsilon_5 \cdot \sin(2\beta^+)]}{c^+ \cdot \sin^2(\beta^+)}, \\
\varepsilon_5 &= -\frac{\beta - \beta^+}{\beta^+}\frac{\pi}{4}, \\
\varepsilon_4 &= \varepsilon_6 = 0.
\end{aligned} \tag{2}$$

To obtain ε_5, the half angle of the monoclinic angular distortion $\beta - \beta^+$ must be considered (all angles in radians) and the negative sign gives an account that shear strains are considered negatives when the angle increases.[48] Null values are assigned to ε_4 and ε_6 shear strains because there are no angular distortions around the x_1' and x_3' axes. The transformation strains for both alloys, CAN4 and CAN19, are summarized in Table II.

In both cases, the lattice enlargement along x_1' and x_3' is accompanied by a shortening in the x_2' direction. Finally, from the values of the transformation strain matrix, we can calculate the Bain matrix, which corresponds to the variant U6 according to the nomenclature given by Bhattacharya in the case of a cubic to monoclinic II transformation.[47] In the case of CAN4, the Bain matrix takes values close to those reported in Ref. 47 using the data from Ref. 49,

$$U_6 = \begin{pmatrix} 1.0647 & 0 & -0.0416 \\ 0 & 0.9241 & 0 \\ -0.0416 & 0 & 1.0243 \end{pmatrix}. \tag{3}$$

Using these values, the Bain matrix for the 12 variant configuration can be obtained following the method and Table 4.4 from Ref. 47. From the above data, a slight increase of the martensite lattice volume with respect the one of the austenite can be calculated, $\Delta V = 0.78\%$, and consequently a compressive state will be developed during the progress of the forward MT, in addition to the local shearing stresses. The level of the internal stresses can be evaluated through the classical equations of elasticity

$$\sigma_i = c_{ij} \cdot \varepsilon_j, \tag{4}$$

$$\varepsilon_i = s_{ij} \cdot \sigma_j. \tag{5}$$

The elastic constants of CAN4 are not available, but those from a closely related Cu-Al-Ni alloy in austenite, at a temperature near the present $M_s = 314$ K, are expected to be a reasonable approach:[50,51] $c_{11} = 138$ GPa, $c_{12} = 122$ GPa, and $c_{44} = 94$ GPa. By using Eq. (4), the stress tensor components become $\sigma_1 = 2.63$ GPa, $\sigma_2 = 0.38$ GPa, $\sigma_3 = 1.98$ GPa, $\sigma_5 = -3.9$ GPa, and $\sigma_4 = \sigma_6 = 0$. These values correspond to the stresses required to transform elastically the austenite lattice to the positions of the martensite lattice, just because of the stress effect without any thermal influence. Obviously, these stresses will never operate because they would produce plastic deformation before inducing the MT and in thermoelastic martensitic transformations, as in the case of most SMAs, the local stresses are strongly reduced thanks to the self-accommodation of martensite variants.[1] Indeed, the experimental stress required to induce the forward MT attains ±0.2 GPa to ±0.4 GPa,[52] being values one order of magnitude lower than those calculated from (4). Nevertheless, the above method can be also used to evaluate the relaxation of the stress and strain fields, during partial transformation cycling (TME and HE), throughout the measurements of the strain evolution accessed by neutron diffraction.

TABLE II. Transformation strains from cubic austenite to monoclinic martensite.

	ε_1	ε_2	ε_3	ε_4	ε_5	ε_6
CAN4	0.0647	−0.0759	0.0243	0	−0.0416	0
CAN19	0.0595	−0.0890	0.0315	0	−0.0361	0

C. Strain evolution during TME and reiterative cycling, the "hammer" effect

As it was commented before, the goal of the present work is to investigate, by neutron diffraction, the influence of the partial thermal transformation (TME) as well as the reiterative partial cycling (HE) on the reverse MT behavior. This experimental information should be useful to evaluate the expected transformation delay, characteristic of the TME and HE, and compare it with previous calorimetric results,[26,27] Along the experimental procedure, described in Fig. 1, martensite and austenite diffraction peak parameters, such as area, height, and FWHM, were carefully analyzed during the MT. The key point is to identify whether the observed evolution could be associated with some relaxation of the internal stress and strain fields, which could be measurable through the proposed neutron diffraction experiments. The Rietveld method[41,42] was used to quantify the amount of each phase fraction and its evolution over the first complete transformation series of spectra presented in Fig. 2. However, when carried out several series of spectra along reiterative cycling, the more simple method to follow the evolution of one

© Author(s) 2019

particular phase is to quantitatively analyze one of the main diffraction peaks of such phase. In the case of CAN4 single crystal, the results depicted in Fig. 4(a) show the estimated percentage of the austenite phase, obtained from the austenite d_{022}-peak area, as a function of temperature, from the martensitic state up to the arrested temperature $T_a = 306$ K. In Fig. 4(a), the six consecutive partial heating runs from 260 K to T_a, according to the schema of Fig. 1, clearly show the progressive decrease of the austenite fraction over the successive heating runs. The transformed mass fraction of austenite at T_a (μ_n^a), as a function of the number of previous partial cycles (n), is shown in Fig. 4(b). A decrease from 61% to about 46% of austenite is measured for CAN4 alloy, whereas a small change, from 56% down to about 50%, is detected for CAN19 alloy. These results are in agreement with previous adiabatic calorimetric measurements[26] and confirm the martensite stabilization produced by partial transformation cycling and consequently the displacement of the remaining reverse MT to higher temperatures. The evolution on cycling will be analyzed in the frame of a thermodynamic model in Sec. IV. As the martensite stabilization on partial cycling is clearly higher in the CAN4 single crystal, we will focus on this alloy for further quantitative analysis of neutron diffraction results. Two approaches will be considered to follow the evolution on cycling: the shift of diffraction peaks in the d-spacing spectra, and the narrowing of the FWHM parameter.

Indeed, diffraction peak position, for some crystallographic directions, shifts toward slightly higher values over reiterative partial cycling. This is clearly seen in Fig. 5 where the peak for the (2 2 1) planes of martensite is plotted at the arrested temperature $T_a = 306$ K for the different partial transformation runs. However, although this peak comes from the martensite lattice, at 306 K, we have a complex microstructural state with a mixture of both martensite and austenite phases. Thus, in order to consider the shift of the peaks to evaluate the relaxation of the strains, it is more convenient to measure such shift of the peaks in a fully martensitic reference state at low temperature, 260 K, after each partial cycle. At this temperature, the shift of the peak positions is smaller but can be still measured by neutron diffraction, and the shift of three martensite peaks (2 2 1), (6 0 0), and (2 0 −2), associated with the relaxation taking place during reiterative cycling is presented in Fig. 6. These shifts mean that the martensite lattice slightly expands parallel to those particular planes becoming less compressed and consequently a relaxation of the local stresses and strains occurs. Through the variation of the d-spaces, with d_0 before any partial run and d_r after six partial cycles, the relaxation of the

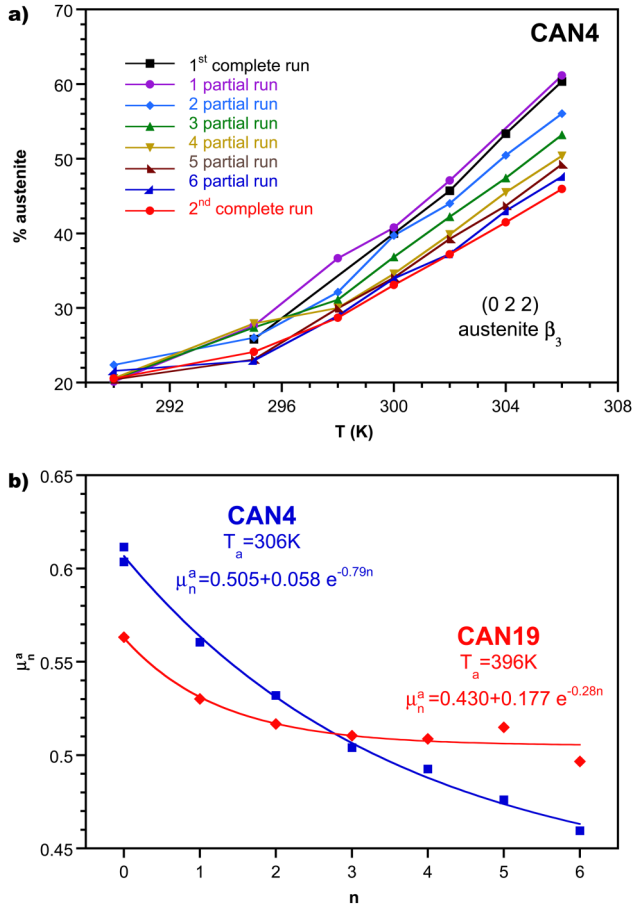

FIG. 4. TME and HE during reiterative partial cycling in CAN4 single crystal and in CAN19 powdered sample. (a) Austenite percentage as a function of temperature along successive partial runs obtained from the d_{022}-peak area in CAN4. (b) Experimental fractional transformed mass μ_n^a at T_a as a function of the previous n partial cycles for both alloys. $T_a = 306$ K for CAN4 (blue) and $T_a = 396$ K for CAN19 (red). The continuous lines are the best fit to exponential laws.

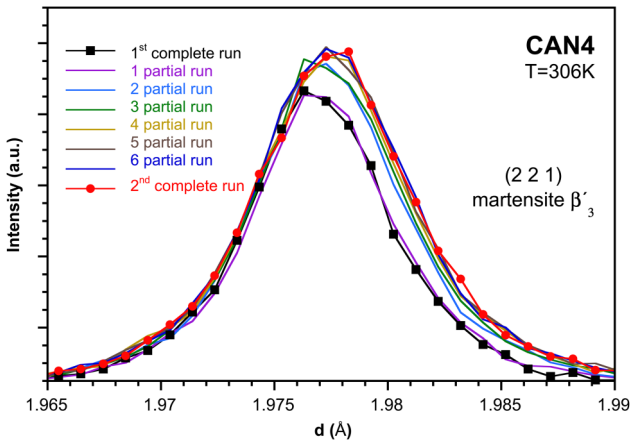

FIG. 5. Neutron diffraction martensite (2 2 1)-peak at the arrested temperature $T_a = 306$ K and its evolution along reiterative partial cycling, HE, in CAN4 single crystal.

© Author(s) 2019

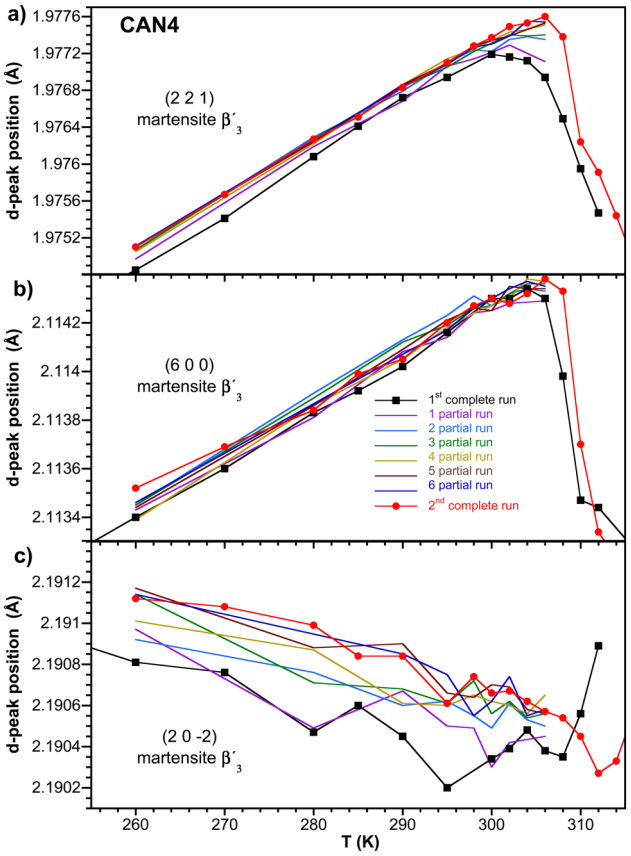

FIG. 6. Evolution of the *d*-peak position shift of three representative martensite reflections in CAN4 alloy: (a) (2 2 1), (b) (6 0 0), and (c) (2 0 −2). Data from two complete heating runs (black and red) and from 6 intermediate partial heating runs up to 306 K are plotted.

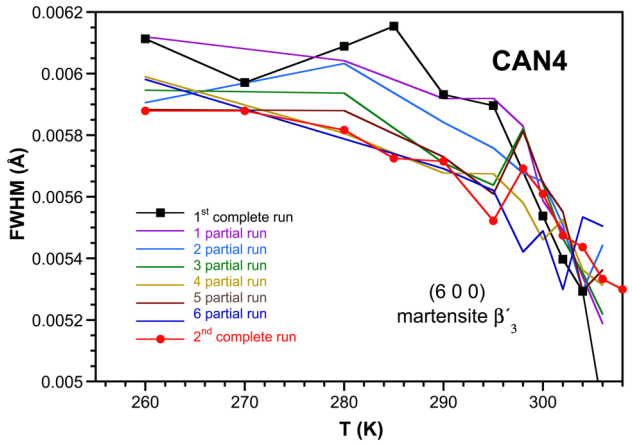

FIG. 7. Experimental FWHM measured for the (6 0 0) martensite peak as a function of temperature, for the different partial cycling runs to study the HE. A 4% decrease of FWHM is observed at 260 K after 6 partial cycles.

strain at 260 K, $\varepsilon_r(hkl) = [d_r(hkl) - d_0(hkl)]/d_0(hkl)$, can be evaluated from each peak shift, $\varepsilon_r(2\ 2\ 1) = 1.2 \times 10^{-4}$, $\varepsilon_r(6\ 0\ 0) = 0.7 \times 10^{-4}$, and $\varepsilon_r(2\ 0\ -2) = 1.4 \times 10^{-4}$; an average value of the relaxed strain $\langle \varepsilon_r \rangle = 1.1 \times 10^{-4}$ can be estimated.

Another method can be used to evaluate the strain relaxation from neutron diffraction data. We have to consider that the strains ε_i defined by Eq. (5) could be either positive or negative, as they depend on the actual values of the local stress field components σ_i. This means that due to self-accommodation of a high number of martensite variants, a continuous distribution of the local strains, including opposite signs, is expected to be present in the martensitic state. The transformation strains are linearly related to the lattice parameters through Eq. (2), which have also a linear dependence on *d*-spaces. As a consequence, a distribution on the strain values means a distribution of the *d*-spaces around its mean position. In this situation, the width of the experimental diffraction peaks, characterized by the FWHM parameter, could be a manifestation of this distribution and used to follow the influence of the transformation cycling.

Even if the relaxation of the strain does not produce any shift of the peak position, the cycling effect would be to sharpen progressively the peaks. This is indeed what is observed in the neutron experiments over the successive partial cycling ($n = 1, \ldots, 6$). As an example, Fig. 7 shows the FWHM evolution of the (6 0 0) martensite reflection, as a function of temperature for the different cycling runs. The FWHM was measured from the corresponding Pearson function (1) fitted to the experimental peak. In spite of some noise, a clear decrease of the FWHM can be seen in all the temperature range from 260 K to 290 K where the sample is in the martensitic state; a decrease of 4% is observed at 260 K. Finally, it should be noted that this effect is not due to any possible instabilities of the neutron beam, since the Cu spectrum, used as control, did not show any significant changes during the experiments.

These results clearly evidence the narrowing of the strain distribution, associated with a relaxation of the high local stresses (positive or negative) produced at the interfaces during the reiterative thermal cycling. The elastic energy stored in both lattices will be accordingly decreased and consequently the structure will lose some of the driving force for the reverse MT, which becomes delayed; the martensite becomes stabilized. Quantifying this effect is a rather tricky task, but it will be approached in Sec. IV.

D. Thermal expansion of the austenite phase

The neutron diffraction technique permits to follow the dependence of d-spacing on temperature even when both phases are present. This fact allows determining the austenite and martensite thermal expansion during the MT. The former

© Author(s) 2019

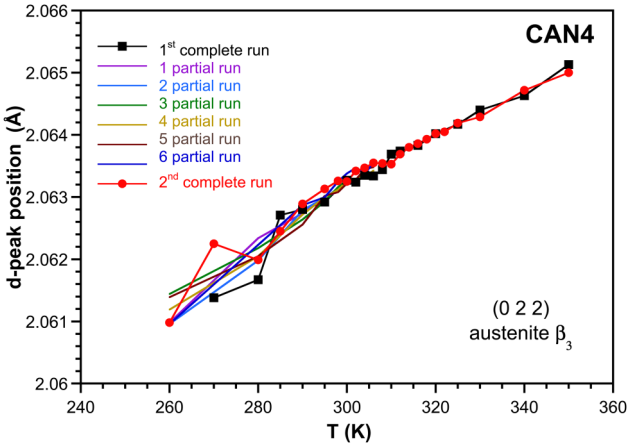

FIG. 8. Austenite (0 2 2)-peak position as a function of temperature. Data from two complete heating runs up to 350 K and from 6 intermediate partial heating runs up to 306 K are plotted. The dispersion approaching 260 K is due to the progressive disappearance of the austenite reflection.

one was studied not only in the pure austenite phase, above A_f, but also throughout the transformation temperature range where both phases are present. In the austenite cubic phase, only one independent thermal expansion coefficient is present, $\alpha = \alpha_{11} = \alpha_{22} = \alpha_{33}$. Figure 8 shows the evolution of the (0 2 2) austenite peak position from 260 K to 350 K in the CAN4 alloy, and α was calculated from the slope of (0 2 2) peak position as a function of temperature. In austenite above A_f, the curve slope is practically constant and leads to $\alpha = 1.70 \times 10^{-5}\ K^{-1}$, in agreement with available data from thermal expansion studies.[53]

E. Thermal expansion of the martensite phase

Contrary to what happens in austenite, the thermal expansion coefficients of the martensite cannot be easily measured by conventional macroscopic techniques, such as dilatometry, and this is the reason why the thermal expansion coefficients of the martensite have not yet been determined. This is again due to the usual presence of self-accommodation variants with different orientations, but this problem can be overcome by neutron diffraction. In Table III, selected martensitic (h k l) peak positions referred to the monoclinic basis (x_1, x_2, x_3) are included. The

TABLE III. Measured directional thermal expansion data (α) for selected martensitic indexed d-peak positions for CAN4 alloy. Planes normal vector components (l_1, l_2, l_3) are referred to the orthogonal crystallophysic base (x'_1, x'_2, x'_3).

	h	k	l	d (Å)	l_1	l_2	l_3	α (K^{-1})
CAN4	2	2	1	1.9753	0.28438	0.7327	0.6195	2.92×10^{-5}
	0	0	2	2.0091	0.0000	0.0000	1.0000	2.32×10^{-5}
	6	0	0	2.1139	0.91216	0.0000	0.4096	9.94×10^{-6}
	2	0	−2	2.1912	0.31553	0.0000	−0.9496	-5.27×10^{-6}

4-independent tensor components (α_{ij}) in the orthogonal monoclinic basis[48] were obtained from

$$\alpha = \alpha_{11} l_1^2 + \alpha_{22} l_2^2 + \alpha_{33} l_3^2 + 2\alpha_{13} l_1 l_3. \tag{6}$$

The corresponding (l_1, l_2, l_3) vector components are defined in the usual orthogonal basis (x'_1, x'_2, x'_3),

$$l_1 = \frac{hbc \sin\beta}{\sqrt{(hbc)^2 + (abl)^2 + (kac \sin\beta)^2 - 2ab^2 lch \cos\beta}},$$
$$l_2 = \frac{kac \sin\beta}{\sqrt{(hbc)^2 + (abl)^2 + (kac \sin\beta)^2 - 2ab^2 lch \cos\beta}}, \tag{7}$$
$$l_3 = \frac{b(al - ch \cos\beta)}{\sqrt{(hbc)^2 + (abl)^2 + (kac \sin\beta)^2 - 2ab^2 lch \cos\beta}},$$

being $x'_1 \equiv x_1$ and $x'_2 \equiv x_2$. The evolution of the peak positions with temperature was exhaustively examined throughout the various heating runs in CAN4 alloy, which are presented in Fig. 6. The slope of these curves determines the directional thermal expansion α values. These results are shown in Table III for some representative examples, corresponding to the three most relevant reflections, (2 2 1), (6 0 0), and (2 0 −2), which are the same presented in Fig. 6 as a function of temperature, plus the reflection (0 0 2). For CAN4, α_{33} is directly determined from the (0 0 2) reflection and the remaining components from the other three reflections cited above.

The tensor diagonalization permits to obtain the eigenvalues or the thermal expansion principal values (α_1, α_2, α_3) and the unitary eigenvectors (e_1^*, e_2^*, e_3^*) defining the tensor principal directions (x_1^*, x_2^*, x_3^*), where x_2^* lies again in the monoclinic binary axis. The obtained results are summarized in Table IV. The fact that $\alpha_{13} > 0$ implies the decrease of the β

TABLE IV. Thermal expansion tensor components (α_{ij}) measured in CAN4 alloy, together with the eigenvectors (e_i^*) and α-zero directions referred to the monoclinic orthogonal basis (x'_1, x'_2, x'_3). The eigenvalues (α_i) are also included.

Phase		Notation	Data
Austenite β_3	Thermal expansion (K^{-1})	α	1.70×10^{-5}
Martensite β'_3	Thermal expansion tensor (K^{-1})	α_{11}	-2.78×10^{-5}
		α_{22}	1.64×10^{-5}
		α_{33}	2.32×10^{-5}
		α_{13}	3.91×10^{-5}
	Eigenvalues (α_i) (K^{-1}): Det(A-αI) = 0	α_1	-4.90×10^{-5}
		α_2	1.64×10^{-5}
		α_3	4.44×10^{-5}
	Eigenvectors(e_i^*): (A-αI) x = 0	e_1^*	(−0.8794, 0, 0.4761)
		e_2^*	(0, 1, 0)
		e_3^*	(−0.4761, 0, -0.8794)
	α-zero directions in $x'_1 - x'_3$ plane		(0.9511, 0, 0.3089)
			(−0.2613, 0, 0.9653)

© Author(s) 2019

monoclinic angle as temperature rises. It is associated with the expansion in the x_3^* direction ($\alpha_3 > 0$) and the shortening in the x_1^* one ($\alpha_1 < 0$). Then, as $\alpha_1 < 0$, the thermal expansion quadric representation is defined by two hyperboloids oriented along x_1^*,

$$\alpha_1(x_1^*)^2 + \alpha_2(x_2^*)^2 + \alpha_3(x_3^*)^2 = 1 \quad \text{(One sheet hyperboloid)}, \tag{8}$$

$$\alpha_1(x_1^*)^2 + \alpha_2(x_2^*)^2 + \alpha_3(x_3^*)^2 = -1 \quad \text{(Two sheets hyperboloid)}, \tag{9}$$

which are depicted in Fig. 9 for the CAN4 alloy. The distance $r = |\vec{r}|$ from the origin to a point of these surfaces represents the α value in the $\vec{r}$ direction, given by $\alpha = \pm 1/r^2$, the sign depending on whether $\vec{r}$ lies on surface (8) or (9), respectively.

Directions for zero-thermal expansion ($\vec{r} \to \infty$) are represented by a conical surface, asymptotic to both hyperboloids, with

$$\alpha_1(x_1^*)^2 + \alpha_2(x_2^*)^2 + \alpha_3(x_3^*)^2 = 0 \quad (\alpha - \text{zero cone}). \tag{10}$$

As α_i values are all different, the three quadrics are elliptical. Analytically, the thermal expansion in any direction $(l_1^*,\ l_2^*,\ l_3^*)$ can be obtained by using the principal values

$$\alpha = \alpha_1 l_1^{*2} + \alpha_2 l_2^{*2} + \alpha_3 l_3^{*2}. \tag{11}$$

As an example, Fig. 10 shows the CAN4 thermal expansion values in the plane orthogonal to the monoclinic axis $(x_1 - x_3)$ where the anticlockwise θ-angle is measured from $x_1' \equiv x_1$. Some important directions, including the principal axes, are

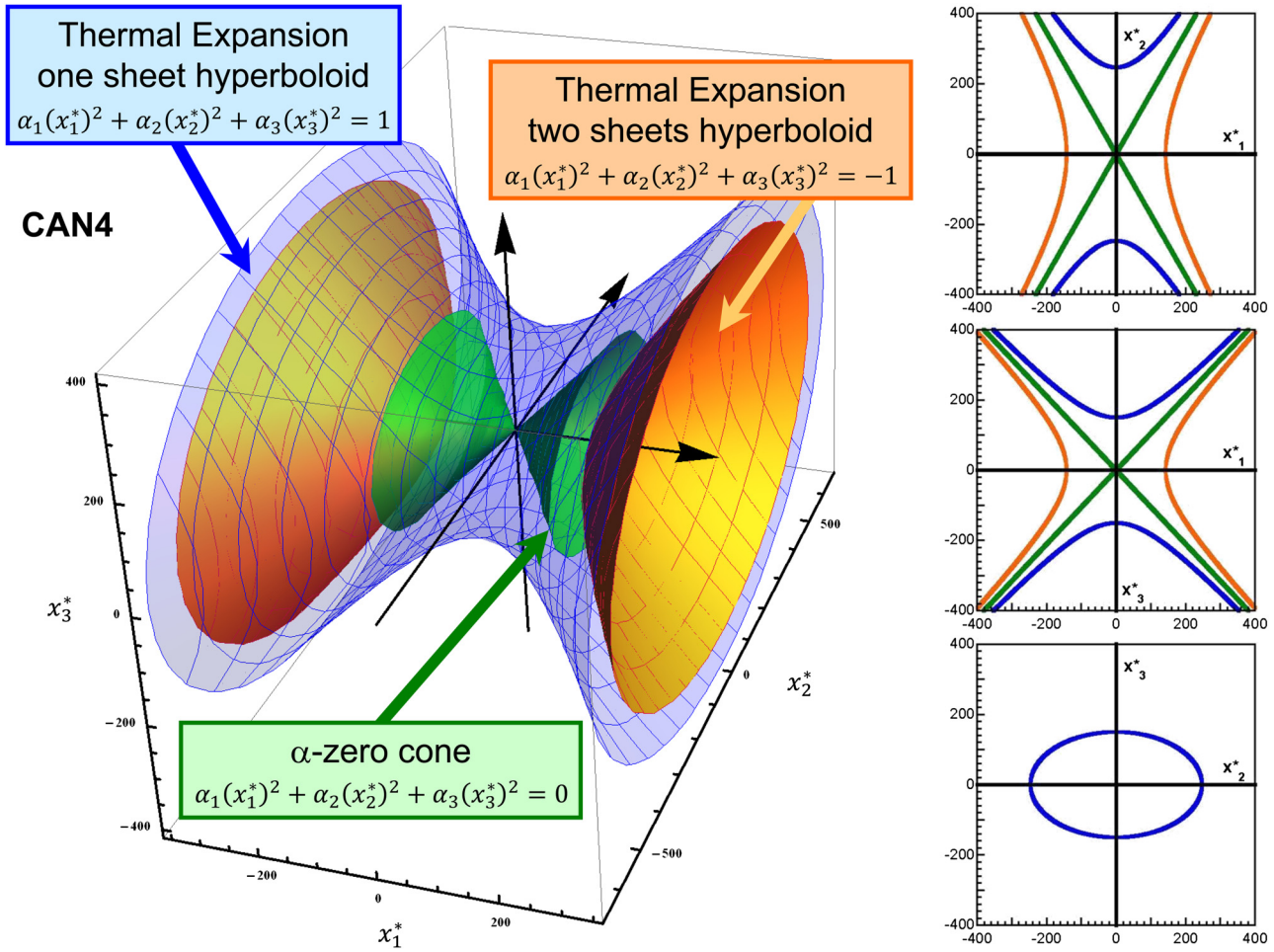

FIG. 9. Thermal expansion quadrics for CAN4 single crystal referred to the principal axes with α-units in K^{-1}. The two hyperboloids associated with positive and negative values of the thermal expansion are shown. The cone surface, which represents directions for $\alpha = 0$, is asymptotic to both hyperboloids and divides both regions. Intersections of these quadrics with the principal planes are also shown.

© Author(s) 2019

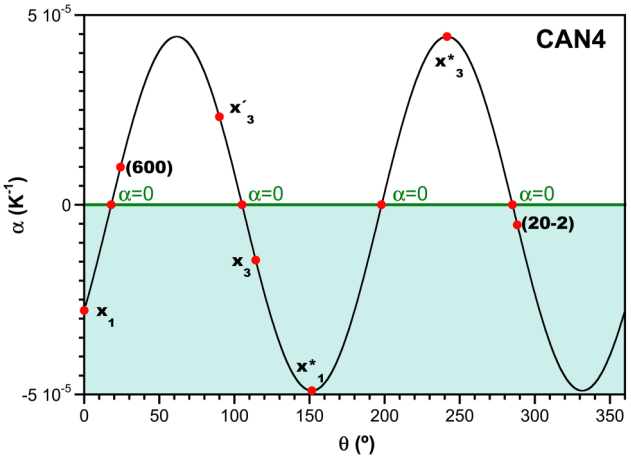

FIG. 10. Directional thermal expansion α in the $x'_1 - x'_3$ plane, measured in the CAN4 alloy. The $\alpha < 0$ regions are shaded in light blue. The anticlockwise θ-angle is measured from $x_1 \equiv x'_1$. Red circles indicate some relevant directions.

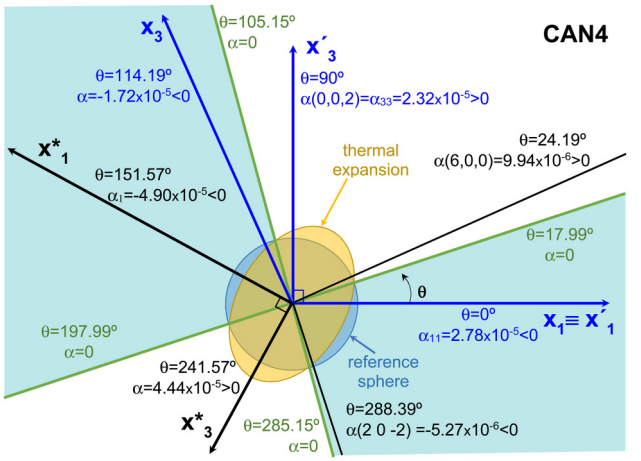

FIG. 11. Representation of the various coordinate systems of CAN4, in a plane orthogonal to the monoclinic axis ($x_2 \equiv x'_2 \equiv x^*_2$) (inwards the page). ($x_1$, x_2, x_3) are the monoclinic crystallographic bases, (x'_1, x'_2, x'_3) are the orthogonal crystallophysic bases used for the α-tensor representation, and (x^*_1, x^*_2, x^*_3) are the thermal expansion principal axes. The anticlockwise θ-angle is measured from $x_1 \equiv x'_1$. Lines in green indicate the α-zero directions. The plane intersections of the α-zero cone (see Fig. 9) and the directions separating the regions for $\alpha > 0$ (in white) and $\alpha < 0$ (in light blue) are shown. Some particular in-plane (h k l) directions and the corresponding experimental thermal expansions are also included. In addition, the plane intersection of the strain ellipsoid ($\varepsilon_i = \alpha_i \Delta T$, for $\Delta T = 1$), which represents the thermal expansion of a unit sphere, is also shown; the actual ellipse axes are approximately enlarged by a factor of 10^3.

identified for CAN4 alloy and plotted in Fig. 11. The relative positions of the various coordinate systems are also shown, as well as the strain ellipsoid, which represents the deformations ($\varepsilon_i = \alpha_i \Delta T$, for $\Delta T = 1$) of a unit sphere,

$$\left(\frac{x_1^*}{1+\alpha_1}\right)^2 + \left(\frac{x_2^*}{1+\alpha_2}\right)^2 + \left(\frac{x_3^*}{1+\alpha_3}\right)^2 = 1. \quad (12)$$

IV. DISCUSSION

The presented results experimentally demonstrate that there is a shift of the neutron diffraction d-spacing along the reiterative partial cycling during the reverse MT (TME and HE), and it was univocally associated with a relaxation of the local stress and strain fields. The cycling procedure of Fig. 1 was specifically chosen to be the same than in previous calorimetric works,[26] and the decrease of the transformed austenite at $T_a = 306$ K as a function of the number of previous partial cycles, presented in Fig. 3(b), exhibits a similar behavior than the one observed by calorimetry,[26] evidencing a direct correlation between both kinds of experiments. A simple thermodynamic model was developed[5] to account for the transformation delay, as a consequence of partial cycling, and offers a consistent explanation of the full set of results obtained by neutron diffraction. Within this model, the total reverse MT, usually extended along a wide temperature range, is considered as a superposition of individual variant phase transitions, at temperatures determined by their particular Gibbs energy $G^*_M = G_M + G_{el}$. Here, G_M is the structural (or the so-called "chemical") Gibbs energy, and G_{el} is related to the individual variant stored elastic energy E_{el} associated with the elastic lattice strains. Thermodynamic theory shows that plates that nucleate at lower temperatures are those that accumulate more elastic energy. Similarly, during the reverse transformation, the greater the elastic energy stored by a martensite plate, the lower its reverse transformation temperature. In other words, the last formed martensites are the first to retransform to austenite. Both single TME and multiple HE account for a progressive elastic energy relaxation when the sample is reiteratively cooled down to martensitic state from the fixed arrested temperature T_a. The successive nucleation processes take place in progressively better accommodation conditions for the variants, and the decrease of the local stresses leads to lower values of the stored elastic energy G_{el}. This elastic energy constitutes the driving force for the reverse MT, and as a consequence, some individual variants become more stable and transform at higher temperatures in successive heating cycles, due to the lower value of G^*_M, which explains the delay of the reverse MT. The stored elastic energy given by the elasticity theory can be expressed by Eq. (13),

$$E_{el} = \frac{1}{2} c_{ij} \varepsilon_i \varepsilon_j. \quad (13)$$

The decrease of the elastic energy is associated to an elastic strain relaxation in agreement with the results from neutron diffraction, where the mean strain relaxation of $\langle \varepsilon_r \rangle = 1.1 \times 10^{-4}$

© Author(s) 2019

was experimentally measured from the shift of the neutron diffraction peaks.

In Sec. III C, the experimental evidence of a decrease of the FWHM due to the narrowing of the distribution associated with each d-spacing was presented, being also associated with the local relaxation of the strained martensite. A simple approach to the strain distribution among the variants is assigning to each ε_i-component, values ranging between two fixed limits $-\varepsilon$ and $+\varepsilon$ around the mean value, which we consider zero for the sake of simplicity. Within this frame, each d_{hkl} is a 4-variable function of ε_i due to Eq. (2) and the relationship between d_{hkl} and the lattice parameters. Each point of the 4-dim variable domain $\varepsilon_i \in (-\varepsilon, \varepsilon)$, characterized by a set (ε_1, ε_2, ε_3, ε_5), represents a particular deformation state $\Sigma\varepsilon$. From this calculation, a histogram of d_{hkl} around its mean value can be obtained. In this simple model, equally probable deformation states $\Sigma\varepsilon$ are considered and the histogram width depends on the selected domain limits $\pm\varepsilon$, which can be chosen from the best fit with experimental data. For example, an empirical value $\pm\varepsilon = 0.0027$ is found adequate to describe the martensite (2 0 −2) diffraction peak of the CAN4 single crystal. In Fig. 12(a), the obtained histogram is compared with the corresponding fitted peak. The height of the histogram is arbitrary and depends on the total number of deformation states taken for calculations, which must be empirically adjusted. In Fig. 12(b), some other histograms calculated in the same conditions are compared with the diffraction spectrum. This simple model allows to evaluate the local strain configuration, even in the absence of any d-peak shift, due to the presence of strained variants of opposite signs.

By decreasing the ε-limit value, we can simulate the progressive reduction of the most strained variants population in the martensitic phase under the successive thermal cycles, together with the associated elastic relaxation during the reverse MT. Unfortunately, the stored elastic energy and its variation under cycling cannot be established by means of Eq. (13), to be compared with the thermodynamic results.[26] Even in the case that the strain tensor (ε_i) could be fully determined, Eq. (13) also requires the precise knowledge of the 13 c_{ij} independent values of the elastic constants in the monoclinic phase, which are experimentally inaccessible due to the small size, large number, and quasi-random orientations of the β'_3 monoclinic variants. For this reason, a simple quasi-isotropic approach with a mean value of the elastic constants of the orthorhombic martensite[54] was considered. By this procedure, we can model the corresponding histograms and compare them with the narrowing of the FWHM measured by neutron diffraction, as shown in Fig. 6, and in parallel verify that the stored elastic energy given by (13) offers a value in agreement with the one measured by calorimetry. Within the frame of this model, the G_{el} drop must be related to the ε distribution narrowing. The model results, for the initial strain distribution $\varepsilon(n = 0) = 0.0027$ and after six partial cycles $\varepsilon(n = 6) = 0.00256$, fit quite well the observed narrowing of the FWHM in the previously selected (2 0 −2) reflection evaluated at 260 K. Then, the application of this simple model to the experimental results offers a reasonable

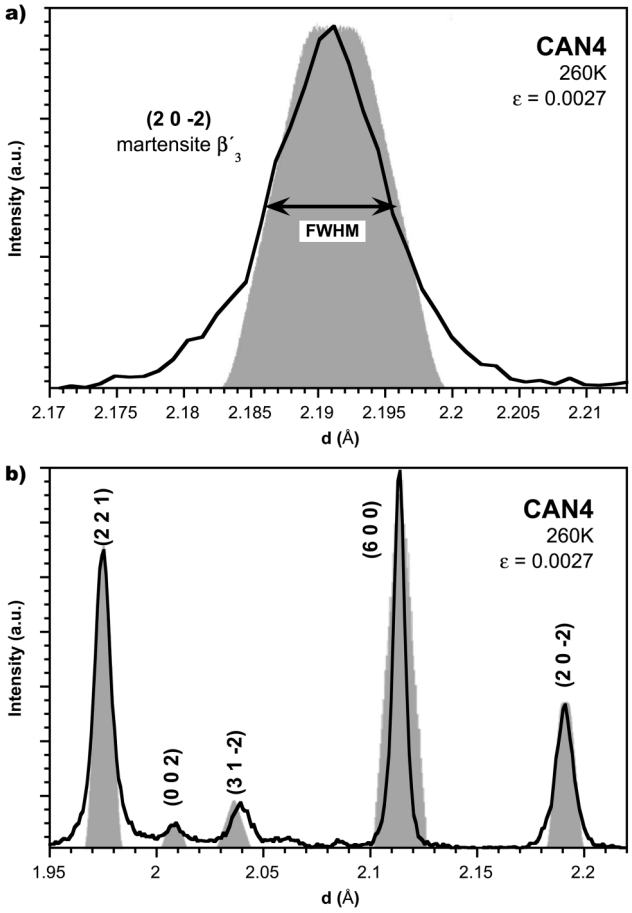

FIG. 12. (a) Theoretical histogram of d_{20-2} (gray) and the corresponding experimental peak (black line) of CAN4 at 260 K. The histogram is calculated for $\varepsilon_i \in (-\varepsilon, \varepsilon)$ with $\varepsilon = 0.0027$ in 0.0001 steps, to fit the experimental peak width. The vertical scale was adjusted to fit the experimental peak. (b) The same comparison for several *h k l* directions.

mean value of the strain relaxation $\langle\varepsilon_r\rangle = \varepsilon(n = 0) - \varepsilon(n = 6) = 1.4 \times 10^{-4}$, comparable to the one measured through the shift of the neutron diffraction peaks.

Before closing this section, the relaxation of strains deserves a still deeper analysis. The average strain relaxation measured by both methods, the shift of peaks position and the narrowing of FWHM, offers a very similar value of $\langle\varepsilon_r\rangle = 1.1 \times 10^{-4}$ and $\langle\varepsilon_r\rangle = 1.4 \times 10^{-4}$, respectively. These values represent the decrease of the strain produced by the relaxation of the stresses generated during the forward transformation and opposing to the nucleation and growing of the martensite. The superposition principle establishes that the local stress field in any point is composed by the addition of the internal plus the external applied stresses. The observed relaxation of the internal stresses (opposing the forward MT) will produce, during the TME, an increase of the reverse transformation

© Author(s) 2019

temperature that should be equivalent to the one expected from the application of the same external stresses promoting the MT, which can be evaluated through the Clausius-Clapeyron diagram. In addition, as the local field stress is unique for both austenite and martensite phases coexisting around the interphase, the relaxation of the stress field can be evaluated through the averaged relaxed strain $\langle\varepsilon_r\rangle$ and Eq. (4). Although the elastic constants of the monoclinic martensite are unknown, they are expected to be close to the ones of orthorhombic martensite, which are also close to those of the austenite phase,[50,54] and in a first approach we can consider the elastic constants of the austenite (given in Sec. III B) to evaluate the stress relaxation through Eq. (4). As it was already commented, the relaxed strains could be of opposite sign depending of the local configuration, and so the sign must be considered in Eq. (4). With these considerations, the measured strain relaxed value $\pm\langle\varepsilon_r\rangle = 1.1\times10^{-4}$ allows to calculate two extreme values of the relaxed stresses between $\sigma_r(\min) = 10.3$ MPa and $\sigma_r(\max) = 40.9$ MPa in austenite. Taking into account the slope of the Clausius-Clapeyron diagram for Cu-Al-Ni between austenite and monoclinic martensite, 2.2 MPa/K,[55] these values of the stress relaxation correspond to a shift of MT, to higher transformation temperatures, ranging between 4.7 K and 18.5 K, in perfect agreement with the calorimetric measurements of the TME in this alloy.[26,28]

Then, we can conclude that the strain relaxation measured by *in situ* neutron diffraction during the TME and HE allows to explain the temperature shift observed on the reverse MT during partial cycling. Or otherwise saying, the shift of the reverse MT observed during partial transformation along the TME and HE effects can be unambiguously attributed to the relaxation of the stress and strain fields, closing the controversy remaining on this matter. Within the frame of this interpretation, it should be noted that TME must not be only present in MTs of shape memory alloys but also in other crystalline materials undergoing structural first order phase transitions with stressed multi-domain microstructures, as was confirmed in a ferromagnetic alloy.[10] In addition, the presented results and analysis help to understand the importance of the stress and strain relaxation even at a small scale and confirm the validity of the argument for stress relaxation at the surface of the pillars as the mechanism responsible for the martensite stabilization in micro/nano pillars.[7,56]

V. SUMMARY

In situ neutron diffraction experiments were performed on two different Cu-Al-Ni samples of slightly different composition and microstructure (a single crystal and a powdered specimen) around the MT, with special emphasis on the temperature memory effects, TME, and HE, taking place during reiterative cycling over a partial thermal reverse MT. This fact, which progressively delays the transformation of the martensite plates to higher temperatures, was previously established by the specific heat behavior.

Neutron diffraction experiments, during similar thermal cycles, show not only the same transformation delay but also allow following the evolution of the elastic stresses through the precise measurement of the local strains relaxation. Two effects have been evaluated. First, the small shift of the diffraction peaks gives account on the strain relaxation in some particular directions. However, in other directions, the presence of plates with opposite strains maintains the diffraction peak positions unaltered, and in this case, a second method to evaluate the strain relaxation was used by measuring the reduction of the strain distribution, which is manifested by the slight narrowing of the peaks (FWHM). The averaged relaxation strain measured by both methods allows to estimate the local relaxation of the stored elastic stresses, which constitute the driving force for the reverse MT during heating. The observed results agree quite well with previous calorimetric experiments in the framework of a simple thermodynamic model and offer a convincing explanation of the sequential character of the MT in a wide temperature range, due to the successive transformations of the individual plates. On thermodynamic grounds, it is a direct consequence of a continuous distribution of the effective Gibbs energy, which determines each plate transformation temperature. In particular, the successive uncompleted thermal cycles promote the relaxation of the elastic stress and strain fields and decrease the elastic contribution to the Gibbs energy of the martensite variants. Moreover, the relaxation of the local stresses can be related, through the Clausius-Clapeyron equation, with the expected shift in temperature during partial thermal transformation cycling; there is a rather good agreement between the neutron diffraction results and previous calorimetric measurements.

In addition, the feasibility of the neutron diffraction techniques to examine the behavior and evolution of lattice parameters, even when several phases are present in the sample, allowed to corroborate the bulk thermal expansion coefficient of the cubic austenite and to establish, for the first time, the values of the thermal expansion tensor coefficients in the monoclinic martensite phase.

In conclusion, *in situ* neutron diffraction allows a complete description of the evolution of the thermo-elastic strains taking place in shape memory alloys (SMAs) along partial thermal transformation. Therefore, TME is expected to be present in multi-domain crystals undergoing structural first order phase transitions (ferroelastic, ferroelectric, etc.) where accommodation processes leading to some strain distribution among domains can take place. These results and methodology open the way to analyze the relaxation of strains in all these multi-domain systems by *in situ* neutron diffraction. Finally, it is worthy of remark that the presented results offer a convincing explanation of the stress relaxation as responsible for some size effects observed at micro/nano scale in SMA and make the point on the physical phenomenon underlying the anomalous behavior observed in SMA during working conditions, involving partial MT, in real applications.

ACKNOWLEDGMENTS

This work was supported by the Spanish Ministry of Economy and Competitiveness (No. MINECO MAT2017-84069-P),

© Author(s) 2019

as well as by the Consolidated Research Group (No. IT-1090-16) and the ELKARTEK-ACTIMAT project from the Education and Industry Departments of the Basque Government. The University of the Basque Country (UPV/EHU) also supported this work with the Research Group GIU17/071. This work has benefited from the use of NPDF at the Lujan Center at Los Alamos Neutron Science Center, funded by the Department of Energy (DOE) Office of Basic Energy Sciences. Los Alamos National Laboratory is operated by Los Alamos National Security LLC, under DOE Contract No. DE-AC52-06NA25396. The upgrade of NPDF was funded by the National Science Foundation (NSF) through Grant No. DMR 00-76488.

REFERENCES

[1]K. Otsuka and C. M. Wayman, *Shape Memory Materials* (Cambridge University Press, 1999).
[2]Z. Nishiyama, *Martensitic Transformation* (Elsevier, 2012).
[3]T. W. Duerig, K. N. Melton, D. Stockel, and C. M. Wayman, *Engineering Aspects of Shape Memory Alloys* (Books on Demand, 1990).
[4]P. Wollants, J. R. Roos, and L. Delaey, Prog. Mater. Sci. **37**, 227 (1993).
[5]J. Rodríguez-Aseguinolaza, I. Ruiz-Larrea, M. L. Nó, A. López-Echarri, and J. San Juan, Acta Mater. **56**, 6283 (2008).
[6]J. San Juan, M. L. Nó, and C. A. Schuh, Adv. Mater. **20**, 272 (2008).
[7]J. San Juan, M. L. Nó, and C. A. Schuh, Nat. Nanotechnol. **4**, 415 (2009).
[8]J. F. Gómez-Cortés, M. L. Nó, I. López-Ferreño, J. Hernández-Saz, S. I. Molina, A. Chuvilin, and J. M. S. Juan, Nat. Nanotechnol. **12**, 790 (2017).
[9]Z. Wang, X. Zu, and Y. Fu, Int. J. Smart Nano Mater. **2**, 101 (2011).
[10]Y. Feng, T. Fukuda, and T. Kakeshita, Intermetallics **36**, 57 (2013).
[11]S. Belyaev, N. Resnina, A. Sibirev, and I. Lomakin, Thermochim. Acta **582**, 46 (2014).
[12]M. Z. Zhou, X. Zhang, X. L. Meng, W. Cai, and L. C. Zhao, Mater. Today Proc. **2**, S867 (2015).
[13]T.-W. Liu, Y.-J. Zheng, and L.-S. Cui, Acta Metall. Sin. Engl. Lett. **28**, 1286 (2015).
[14]I. Ruiz-Larrea, A. López-Echarri, T. Breczewski, G. A. López, I. Lopez-Ferreño, M. L. Nó, and J. M. San Juan, Metals **8**, 246 (2018).
[15]W. A. Johnson, J. A. Domingue, and S. H. Reichman, J. Phys. Colloq. **43**, C4 (1982).
[16]K. Madangopal, S. Banerjee, and S. Lele, Acta Metall. Mater. **42**, 1875 (1994).
[17]G. Airoldi, A. Corsi, and G. Riva, Mater. Sci. Eng. A **241**, 233 (1998).
[18]Y. Zheng, L. Cui, and J. Schrooten, Appl. Phys. Lett. **84**, 31 (2004).
[19]Z. G. Wang, X. T. Zu, S. Zhu, and L. M. Wang, Mater. Lett. **59**, 491 (2005).
[20]X. M. He, J. H. Xiang, M. S. Li, S. W. Duo, S. B. Guo, R. F. Zhang, and L. J. Rong, J. Alloys Compd. **422**, 338 (2006).
[21]N. Liu and W. M. Huang, Trans. Nonferrous Met. Soc. China **16**(Suppl. 1), s37 (2006).
[22]J. Li, Y. Zheng, and L. Cui, J. Mater. Eng. Perform. **19**, 998 (2010).
[23]J. Rodríguez-Aseguinolaza, I. Ruiz-Larrea, M. L. Nó, A. López-Echarri, E. H. Bocanegra, and J. San Juan, Intermetallics **18**, 2183 (2010).
[24]Z. G. Wang, X. T. Zu, H. J. Yu, X. He, C. Peng, and Y. Huo, Thermochim. Acta **448**, 69 (2006).
[25]G. Airoldi, A. Corsi, and G. Riva, Scr. Mater. **36**, 1273 (1997).
[26]J. Rodríguez-Aseguinolaza, I. Ruiz-Larrea, M. L. Nó, A. López-Echarri, and J. San Juan, J. Appl. Phys. **107**, 083518 (2010).
[27]J. Rodríguez-Aseguinolaza, I. Ruiz-Larrea, M. L. Nó, A. López-Echarri, and J. M. San Juan, Acta Mater. **56**, 3711 (2008).
[28]J. Rodríguez-Aseguinolaza, I. Ruiz-Larrea, M. L. Nó, A. López-Echarri, and J. San Juan, Intermetallics **17**, 749 (2009).
[29]J. I. Pérez-Landazábal, V. Recarte, R. B. Pérez-Sáez, M. L. Nó, J. Campo, and J. San Juan, Appl. Phys. Lett. **81**, 1794 (2002).
[30]A. Ibarra, J. San Juan, E. H. Bocanegra, D. Caillard, and M. L. Nó, Mater. Sci. Eng. A **438–440**, 787 (2006).
[31]J. Ye, M. Tokonami, and K. Otsuka, Metall. Trans. A **21**, 2669 (1990).
[32]J. San Juan, R. B. Perez-Saez, V. Recarte, M. L. No, G. Caruana, M. Lieblich, and O. Ruano, J. Phys. IV 05, C8.919–C8.924 (1995).
[33]R. B. Pérez-Sáez, V. Recarte, M. L. Nó, O. A. Ruano, and J. San Juan, Adv. Eng. Mater. **2**, 49 (2000).
[34]V. Recarte, R. B. Pérez-Sáez, M. L. Nó, and J. S. Juan, J. Mater. Res. **14**, 2806 (1999).
[35]J. Rodríguez-Aseguinolaza, I. Ruiz-Larrea, M. L. Nó, A. López-Echarri, and J. San Juan, Acta Mater. **58**, 692 (2010).
[36]A. Ibarra, P. P. Rodríguez, V. Recarte, J. I. Pérez-Landazábal, M. L. Nó, and J. San Juan, Mater. Sci. Eng. A **370**, 492 (2004).
[37]T. E. T. Proffen, Appl. Phys. A **74**, s163 (2002).
[38]T. Proffen and R. B. Neder, J. Appl. Crystallogr. **30**, 171 (1997).
[39]P. F. Peterson, M. Gutmann, T. Proffen, and S. J. L. Billinge, J. Appl. Crystallogr. **33**, 1192 (2000).
[40]C. L. Farrow, P. Juhas, J. W. Liu, D. Bryndin, E. S. Božin, J. Bloch, T. Proffen, and S. J. L. Billinge, J. Phys. Condens. Matter **19**, 335219 (2007).
[41]H. M. Rietveld, J. Appl. Crystallogr. **2**, 65 (1969).
[42]R. A. Young, *The Rietveld Method* (Oxford University Press, 1995).
[43]R. B. Von Dreele, J. Appl. Crystallogr. **30**, 517 (1997).
[44]A. C. Larson and R. B. Von Dreele, GSAS Manual. Los Alamos National Laboratory (Los Alamos National Laboratory, Los Alamos, NM, 1986).
[45]C. Hammond, *The Basics of Crystallography and Diffraction* (Oxford University Press, 2001).
[46]T. Hahn, *International Tables for Crystallography, Volume A: Space Group Symmetry*, 5th revised ed. (Kluwer, 2002), pp. 158 and 282, Corr. 2nd printing (Springer, Dordrecht, 2005).
[47]K. Bhattacharya, *Microstructure of Martensite: Why It Forms and How It Gives Rise to the Shape-Memory Effect* (Oxford University Press, Oxford, 2003).
[48]J. F. Nye, *Physical Properties of Crystals: Their Representation by Tensors and Matrices* (Oxford University Press, 1985).
[49]M. Tokonami, K. Otsuka, K. Shimizu, Y. Iwata, and I. Shibuya, in *Proceedings of the International Conference on Martensitic Transformations ICOMAT 1979, Cambridge, MA, USA, 24–29 June 1979* (Department of Materials Science and Engineering, MIT, 1979), pp. 639.
[50]B. Graczykowski, B. Mroz, S. Mielcarek, T. Breczewski, M. L. Nó, and J. San Juan, J. Phys. D Appl. Phys. **44**, 455307 (2011).
[51]V. Recarte, J. I. Pérez-Landazábal, M. L. Nó, and J. San Juan, Mater. Sci. Eng. A **370**, 488 (2004).
[52]V. Novák, P. Šittner, D. Vokoun, and N. Zárubová, Mater. Sci. Eng. A **273–275**, 280 (1999).
[53]A.S. for M.M.H. Committee, *Metals Handbook. Vol. 2: Properties and Selection: Nonferrous Alloys and Pure Metals* (ASM, 1979).
[54]P. Sedlák, H. Seiner, M. Landa, V. Novák, P. Šittner, and L. Mañosa, Acta Mater. **53**, 3643 (2005).
[55]I. López Ferreño, "Elaboración y caracterización de aleaciones con memoria de forma monocristalinas de Cu-Al-Ni y Cu-Al-Be para altas temperaturas," Ph.D. thesis, Univ. del País Vasco UPV/EHU, Leioa, Spain, 2015.
[56]J. F. Gómez-Cortés, M. L. Nó, A. López-Echarri, I. Ruiz-Larrea, T. Breczewski, and J. M. San Juan, Phys. Status Solidi A **215**, 1800340 (2018).

© Author(s) 2019